Large-Area Si-Doped Graphene: Controllable Synthesis and Enhanced Molecular Sensing

Ruitao Lv, Maria Cristina dos Santos, Claire Antonelli, Simin Feng, Kazunori Fujisawa, Ayse Berkdemir, Rodolfo Cruz-Silva, Ana Laura Elías, Nestor Perea-Lopez, Florentino López-Urías, Humberto Terrones, and Mauricio Terrones**

Following the isolation of graphene in 2004,[1] the idea of doping graphene emerged and it is now possible to alter the electronic and chemical properties of graphene by using this approach. In recent years, graphene doping has become a very hot topic and reviews summarizing recent achievements can be found in the literature.[2] Based on the way the Fermi level shifts, doped graphene could be classified into two main categories: i) electrical doping, such as gate-controlled doping,[3] metallic cluster-induced doping[4] or substrate-induced doping;[5] and ii) chemical doping, such as substitutional doping with heteroatoms,[6] or molecular doping[7]. In particular, substitutional doping is a very stable way to tailor the electrical and chemical properties of graphene. Due to the size limitation, the most adjacent neighbors of carbon in the periodic table of the elements, i.e., boron and nitrogen, are the best choice for achieving substitutional doping due to their similar sizes when compared with carbon. Accordingly, both experimental and theoretical research on N-doped and B-doped graphene have been extensively carried out.[8] For other adjacent atoms (e.g., S, P, Si), the substitutional dopants will protrude out of the graphene plane due to the size limitation effect.[9] So far, S-doped[10] and P-doped[11] graphene have been experimentally obtained. However, to the best of our knowledge, Si-doped graphene (SiG) has not been intentionally synthesized so far. Nevertheless, Chisholm et al. successfully identified Si atoms in the graphene lattice with annular dark-field (ADF) imaging in a scanning transmission electron microscope. The source of Si dopants in their case is likely the glassware used to process graphene oxide.[12] In addition, during the chemical vapor deposition (CVD) growth of pristine (or undoped) graphene, Si impurities derived from the quartz tube reactor or SiO_2/Si wafers can also be occasionally detected in the final products, but this is not a controllable approach for producing SiG.[13] Furthermore, SiG might possess unique and attractive properties, as predicted by theoretical calculations.[13,14] For instance, density functional theory (DFT) calculations demonstrated that SiG can be used as an efficient metal-free catalyst for oxygen reduction reactions (ORRs),[15] nitrogen monoxide (NO) reduction,[16] etc. Si-doping in graphene has been theoretically predicted to increase the amount of physisorbed hydrogen dramatically. For example, 10 at% Si-doping in graphene could increase the hydrogen storage capacity from 0.8 to 2.4 wt%, thus showing great potential in storing hydrogen.[17] In addition, when compared with pristine graphene (PG), SiG could serve as a more efficient gas sensing material because it is significantly more reactive when absorbing some toxic molecules, such as CO and NO_2.[18]

Graphene-enhanced Raman scattering (GERS) is now becoming a useful technique for detecting trace amounts of organic molecules, which is inspired by surface-enhanced Raman scattering (SERS), although it is driven by a different mechanism.[19] PG has been proved to be an excellent SERS substrate that can efficiently suppress the fluorescence background from some organic molecules (e.g., rhodamine 6G, protoporphyrin IX)[20]. Furthermore, our recent work has demonstrated that the substitutional doping of graphene with heteroatoms

Dr. R. T. Lv
Key Laboratory of Advanced Materials (MOE)
School of Materials Science and Engineering
Tsinghua University
Beijing 100084, China
E-mail: lvruitao@tsinghua.edu.cn
Prof. M. C. dos Santos
Instituto de Física
Universidade de São Paulo
05508-090, São Paulo, SP, Brazil
Dr. C. Antonelli
Department of Materials Science & Engineering
Universidad Carlos III de Madrid
Madrid, Spain
S. M. Feng, Dr. K. Fujisawa, Dr. A. Berkdemir, Dr. A. L. Elías, Dr. N. Perea-Lopez, Prof. M. Terrones
Department of Physics and Center for 2-Dimensional and Layered Materials
The Pennsylvania State University
University Park, PA 16802, USA
E-mail: mut11@psu.edu
Prof. R. Cruz-Silva, Prof. M. Terrones
Institute of Carbon Science and Technology
Shinshu University
Wakasato 4–17–1, Nagano 380-853, Japan
Prof. F. López-Urías
Advanced Materials Department
IPICYT, Camino a la Presa San José 2055
Col. Lomas 4a sección, San Luis Potosí S.L.P., 78216, México
Prof. H. Terrones
Department of Physics
Advanced Physics and Astronomy
Rensselaer Polytechnic Institute
100 Eighth Street, Troy, NY 12180, USA
Prof. M. Terrones
Department of Chemistry
Department of Materials Science and Engineering
The Pennsylvania State University
University Park, PA 16802, USA

DOI: 10.1002/adma.201403537

(e.g., nitrogen) can remarkably enhance the GERS.[8d] As mentioned above, Si-doping could favor the enhanced adsorption of different molecules onto graphene, and thus may lead to a significant improved GERS effect. However, due to the inaccessibility of large-area SiG sheets, there are almost no reports on the GERS effect using SiG. In this work, we report a facile and controllable synthesis of large-area SiG sheets for the first time using a bubbler-assisted ambient-pressure chemical vapor deposition (AP-CVD) setup. Their excellent GERS characteristics were demonstrated using crystal violet (CRV), rhodamine B (RhB) and methylene blue (MB) as probe molecules. This enhanced GERS signal of SiG was elucidated using ab initio calculations.

Large-area SiG sheets were synthesized using methoxytrimethylsilane (MTMS, $C_4H_{12}OSi$) and hexane as silicon and carbon precursors, respectively. The vapor of liquid precursors (MTMS + hexane) was transported to the CVD reactor by bubbling argon. The feeding rate of precursors can be well controlled by bubbling gas with a mass flow controller (MFC). Copper foils (99.8% purity, 25 μm thick) were used as substrates for the growth of SiG. More details can be found in the Experimental Section and Figure S1 in the Supporting Information. **Figure 1**a depicts a typical photograph of a SiG sheet grown on a copper substrate. Due to the high transparency of the SiG monolayer, as-grown specimens show almost the intrinsic appearance of original copper foil. More importantly, the SiG sheets can be easily transferred from the foils to different substrates, such as SiO_2/Si wafers, quartz slides, etc. With the protection of polymethyl methacrylate (PMMA) layers, the size and shape of transferred SiG sheets can be preserved and controlled. Figure 1b,c show the SiG sheets with ca. 2 cm × 2 cm size onto a SiO_2/Si wafer and a quartz slide, respectively. In particular, as-synthesized SiG sheets exhibit homogeneity and transparency, which can be clearly seen from Figure 1b,c. A transmission electron microscopy (TEM) image of SiG sheets is shown in Figure 1d. Even with a PMMA-free transfer method, large-area SiG sheets can still be obtained on TEM grid except for a small crack (highlighted with green color) in a suspended area, as shown in Figure 1d. The corresponding selected-area electron diffraction (SAED) pattern of monolayer SiG sheet clearly shows the hexagonal graphene

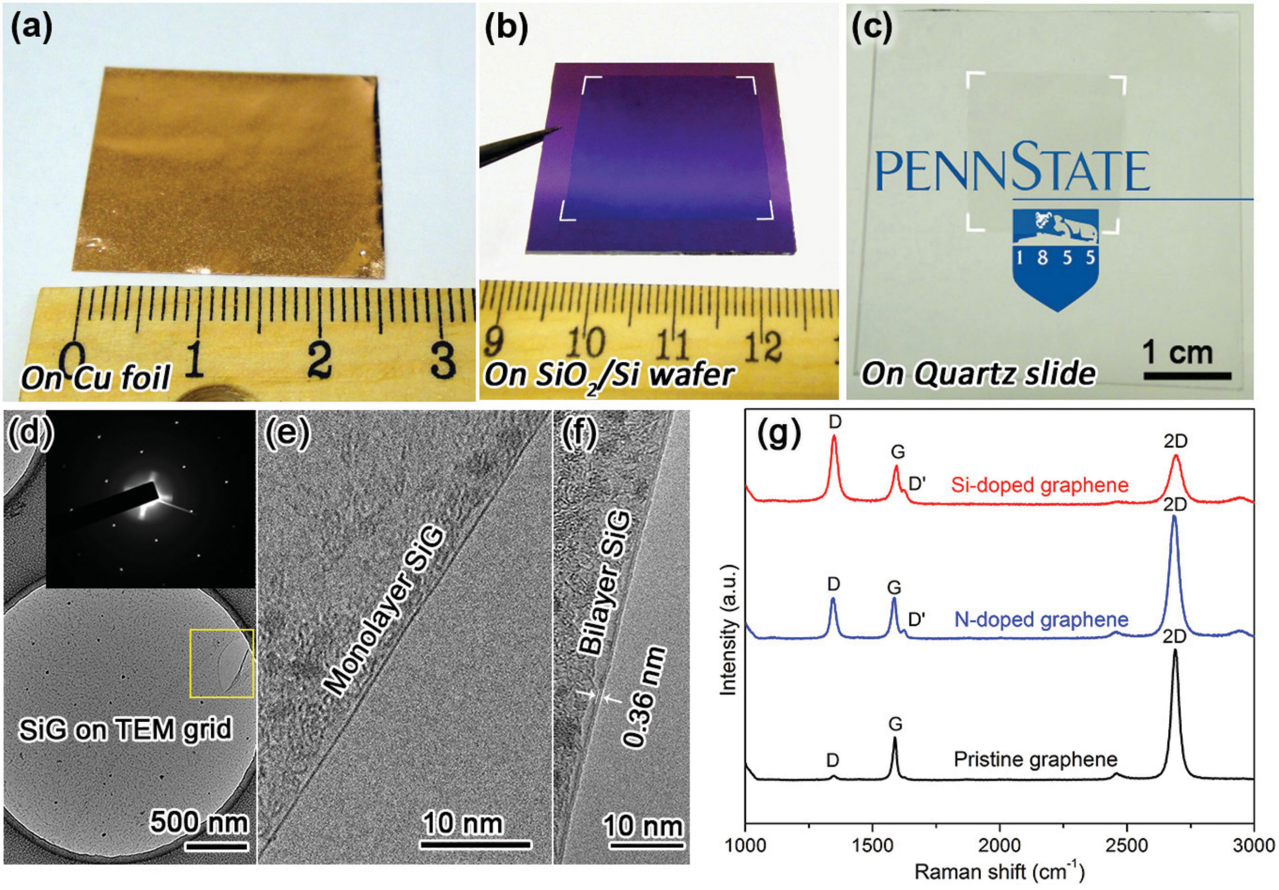

Figure 1. Si-doped graphene (SiG) sheets on different substrates and their typical Raman spectra. a) A photograph of as-grown SiG on copper foil. b) As-transferred SiG sheet on a SiO_2/Si wafer. The scale unit of the ruler shown in (a) and (b) is cm. c) As-transferred SiG on a quartz slide is highly transparent. The logo of Penn State underneath the SiG sheet can be clearly seen. d) Transmission electron microscopy (TEM) image of as-transferred SiG sheet on gold TEM grid. The inset is the corresponding selected-area electron diffraction (SAED) pattern of monolayer SiG. e) Monolayer and f) bilayer SiG sheets on TEM grid. The images were taken at the folded edges highlighted in (d) with the yellow square. g) Typical Raman spectrum of SiG sheet on SiO_2/Si substrate. The Raman spectra of pristine and nitrogen-doped graphene are also shown here for comparison. Compared with pristine graphene (PG), an increased D-band and a decreased 2D-band are the features of SiG sheets, which might be attributed to the graphene lattice distortion caused by Si doping.

honeycomb (see inset in Figure 1d and the corresponding image in Figure 1e). In addition, bilayer SiG sheets can be occasionally detected by high-resolution TEM (HRTEM), as shown in Figure 1f, which was taken at the folded edges highlighted in Figure 1d with a yellow square. The interlayer distance of bilayer SiG is about 0.36 nm (Figure 1f), which is close to the thickness of monolayer graphene (0.35 nm). Atomic force microscope (AFM) image of as-transferred SiG sheet on a SiO_2/Si substrate was shown in Figure S3 in the Supporting Information. It also confirmed that most of the regions in as-obtained SiG sheets are monolayer graphene with thicknesses no more than 1.0 nm, except for some few-layer islands. Figure 1g shows the typical Raman spectrum of as-transferred SiG sheets on SiO_2/Si substrates. For comparison, we synthesized PG and nitrogen-doped graphene (NG) sheets as control samples. Figure 1g shows characteristic features for SiG. One is the presence of a strong D-band (ca. 1347 cm^{-1}), and another is the prominent D'-band (ca. 1625 cm^{-1}), both absent in PG. This D-peak in graphene is usually caused by the breathing modes of six-atom rings and a defect is necessary for its activation.[21] In addition, the D'-peak can be attributed to the double resonance occurring as an intravalley process.[21] In the present case, the Si-dopant may cause a slight distortion of the graphene lattice, thus leading to a stronger D-band than that of PG. Interestingly, the D-band, G-band and 2D-band frequencies do not shift significantly when compared to PG (Figure 1g). Previous work has shown that the 2D band responds differently to hole and electron doping. As shown in Figure 1g, a remarkable downshift (ca. 7 cm^{-1}) of the 2D band position can be detected in NG sheets when compared with that of PG and SiG. Even though there is no obvious peak position difference between SiG and PG Raman modes, the relative intensities of the D-band and 2D-band behave quite differently when they are normalized with the G-band intensity (I_G). Figure S2 in the Supporting Information shows the statistical analysis of I_D/I_G and I_{2D}/I_G of SiG samples synthesized with different MTMS concentrations. Here I_D and I_{2D} correspond to the D-band and 2D-band intensities, respectively. When the concentration of MTMS in hexane is 0, the as-synthesized sample will actually be PG. As shown in Figure S2 in the Supporting Information, the I_D/I_G value increases with the increase of MTMS concentration. In particular, when the concentration of MTMS/hexane is 2 μL/mL (0.2% volume concentration), the average I_D/I_G value reaches a plateau. In addition, the I_{2D}/I_G value decreases with increasing the MTMS concentration, and reaches the minimum when the concentration of MTMS/hexane is 2 μL/mL. As demonstrated in previous work, the higher I_D/I_G and lower I_{2D}/I_G values might lead to a more effective substitutional doping.[8d] Therefore, we fixed the MTMS concentration at 2 μL/mL for the rest in order to achieve a fairly high Si doping level within graphene.

In order to know the distributions of I_D/I_G and I_{2D}/I_G values in a large area, we recorded Raman mapping on the SiG sample synthesized with 2 μL/mL MTMS/hexane. As shown in **Figure 2**a, more than half of the measured area shows I_D/I_G values larger than 1.0, except for the dark regions. More interestingly, the yellow sections (I_D/I_G > 1.5) shown in Figure 2a

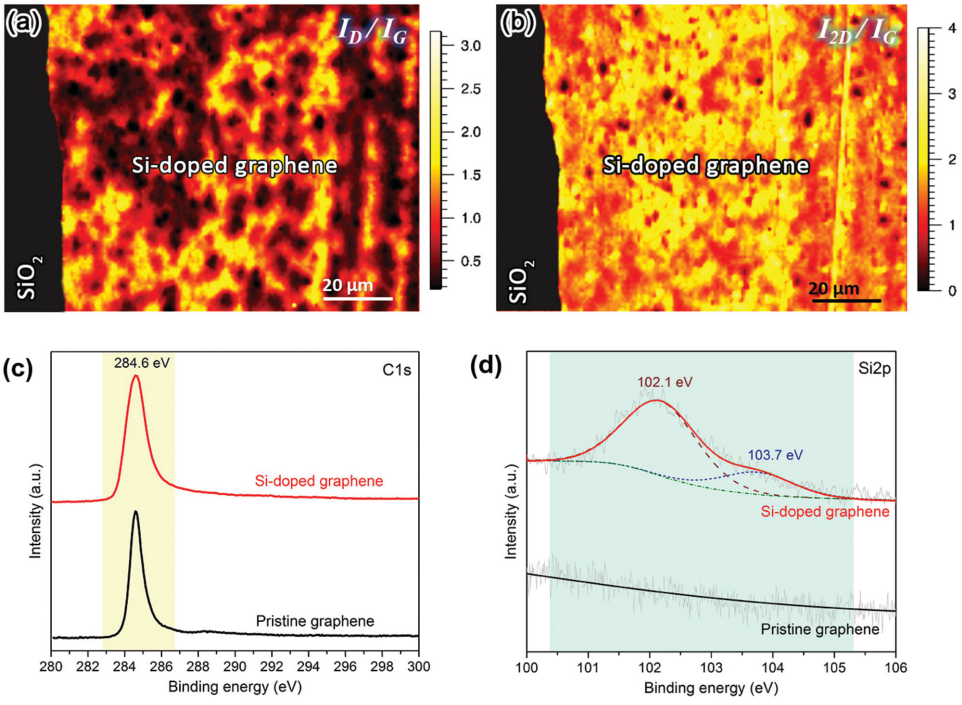

Figure 2. Raman mapping and X-ray photoelectron spectroscopy (XPS) characterizations of as-synthesized SiG sheets. a) D-band over G-band intensity ratio (I_D/I_G) mapping and b) 2D-band over G-band intensity ratio (I_{2D}/I_G) mapping of NG on a SiO_2/Si substrate. Most of the area shows I_{2D}/I_G ratio more than 2, which is in accordance with that shown in Figure 1g. c) XPS C1s fine scan of Si-doped and pristine graphene. The main peak at 284.6 eV corresponds to the graphite-like sp^2 C. d) Si2p fine scan of SiG and PG sample. The green line exhibits the Shirley background. The XPS measurements for different graphenes were all carried out on copper foils instead of SiO_2/Si wafers to avoid the Si signals from substrates. In the case of SiG, the Si2p line can be deconvoluted into two component peaks located at 102.1 eV and 103.7 eV, respectively.

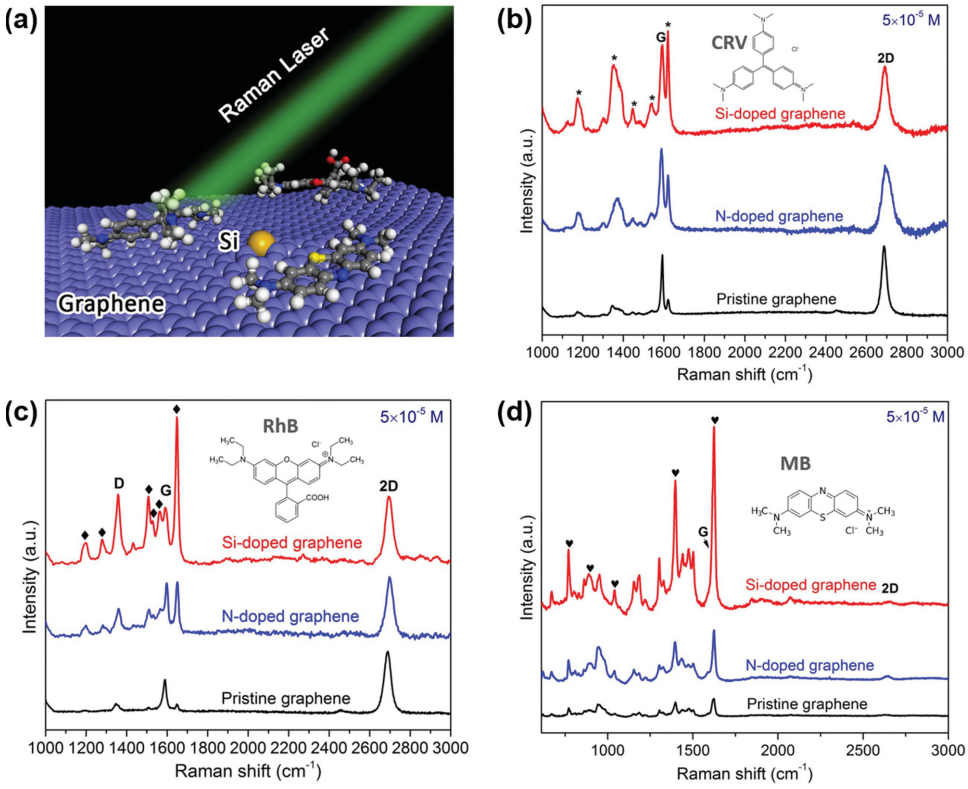

Figure 3. Enhanced Raman scattering effect of SiG sheets for probing different dye molecules. a) Schematic illustration of SiG and different probe molecules, that is, crystal violet (CRV), rhodamine B (RhB) and methylene blue (MB). The laser lines are 514 nm for the cases of CRV and RhB, and 647 nm for MB. b–d) Raman signals of (b) CRV, (c) RhB and (d) MB molecules on pristine, N-doped and Si-doped graphene sheets. The probe molecule concentrations are all 5×10^{-5} M. The integration time is 10 s for all cases. The peaks marked with "*", "♦" and "♥" are the corresponding signals from CRV, RhB and MB molecules, respectively.

turn to reddish orange ($I_{2D}/I_G < 1.5$) in Figure 2b. As pointed out in previous work, the 2D band is the second order of the D peak. For a "defect-free" monolayer PG, the I_{2D}/I_G is usually quite high (more than 4).[22] In our case, the increased I_D/I_G and the decreased I_{2D}/I_G might be attributed to the Si atoms doping the graphene lattice. The presence of Si was confirmed using X-ray photoelectron spectroscopy (XPS). In order to rule out the effect of the substrate, XPS measurements for different graphenes were all carried out on the native substrate (i.e., copper foil) instead of SiO_2/Si wafers, thus avoiding the Si signals from substrates. As shown in Figure 2c, both SiG and PG display prominent peaks at ca. 284.6 eV, which corresponds to the graphite-like sp^2 hybridized carbon. At ca. 102.0 eV, a clear peak arising from Si can be observed in the SiG sample, while this peak is absent for PG (see Figure 2d). Moreover, the Si2p line can be deconvoluted into two component peaks located at 102.1 eV and 103.7 eV, respectively. In particular, the peak located at 102.1 eV might be a feature of silicon binding to carbon in the forms of a single silicon atom or a small silicon cluster. Based on our XPS analysis, the Si doping level in as-synthesized SiG is ca. 1.75 at%. Furthermore, the Si doping levels in SiG sheets can be controlled by varying the MTMS concentrations, as shown in Figure S4 in the Supporting Information.

Si-doping can not only affect the Raman responses of graphene itself, but can also lead to a significantly enhanced GERS effect for detecting some organic (fluorescent) molecules. We have tried different dyes as probing molecules that include crystal violet (CRV), rhodamine B (RhB) and methylene blue (MB). Due to their strong fluorescence, these organic molecules cannot be detected by Raman spectroscopy when deposited on bare SiO_2/Si substrates. Both the Zhang group's pioneering work[19,20] and our previous report[8d] have clearly demonstrated that PG can serve as a good substrate for enhancing the Raman scattering signals of organic molecules by quenching the fluorescence. Furthermore, we have demonstrated that N-doping in graphene can lead to an enhanced Raman scattering when compared to PG.[8d] Even more remarkably, when we use SiG as substrate, a significantly stronger GERS effect can be observed for different molecules when compared to both pristine and N-doped graphenes (see **Figure 3**). All the peaks are normalized against the intensity of the 520 cm^{-1} mode of Si coming from the substrate. Figure S5–S7 in the Supporting Information show the I_{SiG}/I_{PG} and I_{NG}/I_{PG} comparisons for different probe molecules. Here I_{SiG}, I_{NG}, and I_{PG} denote the corresponding peak intensity of probe molecules on Si-doped, N-doped and pristine graphene, respectively. Based on Figure 3 and Figure S5-S7, the following features should be emphasized: i) probe molecules on chemically doped graphenes (e.g., NG, SiG) show clear enhanced Raman scattering when compared to those on pristine graphene (additional vibration fingerprints of probe molecules that are not observed when using undoped graphene as a substrate, could be clearly detected), and ii) Si-doping leads

to a remarkably improved GERS effect when compared to NG. The intensities of all the Raman peaks from different probe molecules (e.g., CRV, RhB, MB) are remarkably improved and clearly resolved.

As mentioned above, GERS is actually inspired by the surface-enhanced Raman scattering effect although the mechanism of GERS is still not yet fully understood. In order to elucidate the GERS mechanism, we carried out electronic structure calculations of SiG sheets and the interactions of RhB with different SiG substitution geometries. We calculated the graphene substrate as a 10 × 10 hexagonal network of carbon atoms (200 carbon atoms) with zigzag edges saturated with hydrogen atoms. Three different Si substitution cases were considered: (*Si3*) one carbon atom is substituted by a silicon atom; (*Si4*) two carbon atoms are substituted by a single silicon atom, and (*SiO*) one carbon atom is substituted by a Si–O group. The geometry associated with the *Si3* scheme is the most intuitive, in which silicon binds to three neighboring carbon atoms; the other two doping configurations, *Si4* and *SiO*, were also considered for comparison purposes, especially because the former has been recently observed in non-intentionally doped graphene whereby the silicon atom is imaged bonded to four carbon atoms.[13] The third configuration (*SiO*) was studied because oxygen is a common contaminant and Si–O bonds are likely to form (from the XPS analysis, Si 2p binding energy is the same as found in polysiloxanes and aromatic siloxane copolymers.[23])

In the present study, RhB was assumed in its cationic form, RhB^+, which is dissociated from Cl^-. The adsorption of RhB^+ on PG and over the Si-doped systems *Si3*, *Si4* and *SiO*, was studied in the framework of van der Waals corrected Density Functional Theory (DFT-D) as proposed by Grimme,[24] and adopting the hybrid B3LYP functional.[25] Optimized geometries are shown in **Figure 4**a–d. The PG surface (Figure 4a) remains planar after RhB^+ adsorption, differently from the Si4 case shown in Figure 4d, which stabilizes into a planar geometry in the absence of the dye molecule but adopts a concave curvature around the Si4 site upon the molecule adsorption. *Si3* and *SiO* doping configurations are depicted in Figure 4b,c, respectively, and result in convex surfaces caused by the trigonal structure and the presence of longer C-Si bonds when compared to C–C bonds. This doping induced convex curvature is beneficial for enhancing the dye interaction with the graphene surface in view of the geometry of RhB^+, which contains the benzoic acid group rotated by an angle close to 90° with respect to the xanthene ring. The induced curvature in the *Si3* or *SiO* cases also allows the wrapping of RhB^+ around the defective site, exhibiting a stronger interaction between the adsorbate and the substrate.

The electronic structures of the studied graphene sheets, in the form of densities of states obtained from the Kohn–Sham eigenvalues, are displayed in Figure 4e. The Fermi energy of PG was taken as the zero reference. While PG and Si3 exhibit both the same Fermi energy, an energy shift to lower values was observed for the other doped cases (–0.10 eV for *Si4* and –0.13 eV for *SiO*). The densities of states are very similar, but the most important differences appear around the Fermi level. This is due to localization of electronic states induced by the defective sites. The adsorption of RhB^+ produces a polarization of the surface and a small charge transfer, in the range $-0.09e$ to $-0.18e$ (e is the electronic charge), with the smallest value corresponding to the *Si3* substrate. The interaction of this dye with the different doped graphene sheets can also be evaluated by the positioning of the frontier orbitals (the highest occupied and the lowest unoccupied Kohn–Sham orbitals, here referred to as HOMO and LUMO, respectively) in the energy spectrum. These orbitals interact with the quasi-continuum of states of the substrates, changing their relative position with respect to the Fermi energy of the substrate, and spreading into several states that correspond to mixtures of the HOMO (LUMO) as well as states present in the doped and undoped graphene sheets. The energy spectrum associated with the HOMO and LUMO levels of RhB^+ relative to the Fermi energy of the system (graphene and dye) is depicted in Figure 4f–i. Here, the reference is the Fermi energy of the RhB^+/PG system. The vertical black arrows show the position of the Fermi energy for each case. The taller vertical bars represent the energy of the orbitals that are mostly localized on the dye while the shorter bars represent the mixed states having a significant contribution from the HOMO or LUMO orbitals of RhB^+. It is evident that the *Si3* type stabilizes the LUMO level with respect to graphene and that the spreading of the HOMO is larger and closer to the Fermi energy. The *Si4* and *SiO* cases place the LUMO far from the Fermi level. The dye HOMO-LUMO energy gap is approximately the same for RhB^+ adsorbed on PG, *Si3* and *Si4* and it is reduced in the case of *SiO*.

The GERS measurements described above showed that PG is able to enhance the Raman activity of the dye molecules adsorbed on its surface and that SiG further enhances the Raman scattering. By comparing the electronic structure of the different graphene sheet models, it seems reasonable to assume that the LUMO level of the adsorbate should lie close to the Fermi energy in order to achieve GERS sensing. As shown in Figure 3, nitrogen-doped graphene exhibits reasonable molecular sensing properties when compared to PG. Substitutional nitrogen does not significantly alter the graphene lattice and works as an electron donor, causing a shift of NG Fermi energy towards higher energies when compared with PG, thus approaching the Fermi energy and the LUMO level of the dye. It is important to discuss the strength of the interaction between the adsorbate and the graphene surface: RhB^+ bonding to the Si site in the *Si3* model is stronger than that obtained in all the other cases, as indicated in Figure 4f– 4i. The increased sensing ability of Si-doped graphene towards CRV, RhB and MB could be an indication of this strong interaction. Among the studied dyes, CRV possesses a non-planar geometry, which prevents strong interactions with a nearly flat surface. RhB contains a benzoic acid group that is twisted with respect to the xanthene ring, and MB does not suffer from steric hindrance constraints and can lie flat on the surface, or wrap around a Si site as RhB. It is important to consider the laser excitation energy used in these experimental measurements. The excitation energy needs to be nearly in resonance with the HOMO-LUMO gap of the adsorbed molecule. We noted that the best sensing results were achieved using the 514.5 nm laser line for CRV and RhB, and with the 647 nm laser for MB.

The GERS mechanism of the organic dyes could thus be pictured as an electronic excitation of graphene (or doped graphene) that is transferred to the dye molecule through the polarization of the surface and the adsorbate-substrate

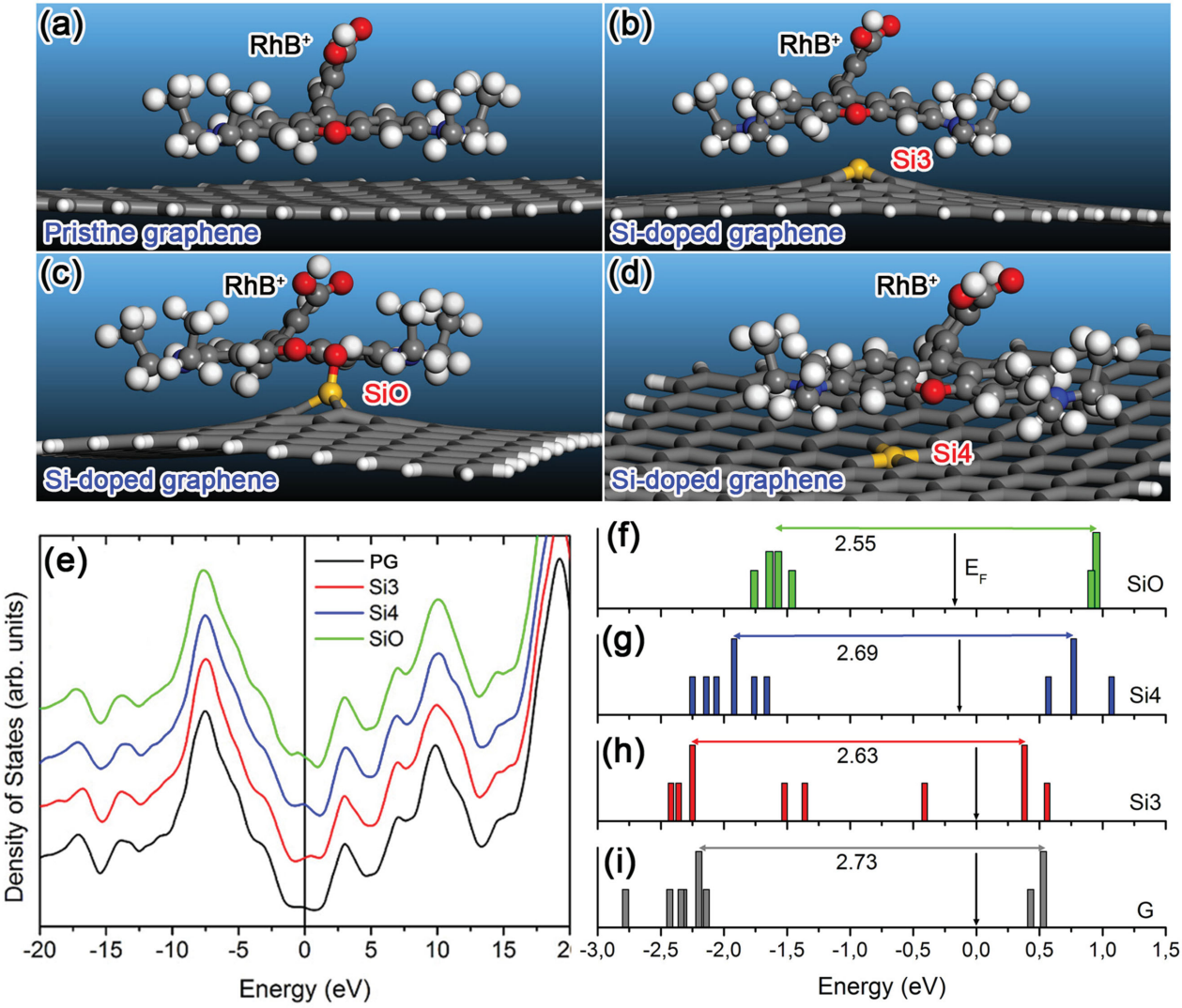

Figure 4. Optimized geometries of RhB^+ adsorbed on (a) PG and different Si-doped graphene sheets (b–d): b) *Si3*: one carbon atom is substituted by a silicon atom; c) *SiO*: one carbon atom is substituted by a Si–O group; and d) *Si4*: two carbon atoms are substituted by a single silicon atom. Color scheme: gray = carbon, orange = silicon, red = oxygen, blue = nitrogen, white = hydrogen. e) Densities of states of different graphene sheets. The curves are shifted upwards for clarity. f–i) Spreading of the HOMO and LUMO energy levels of RhB^+ interacting with different graphene sheets. The Fermi energy of PG was taken as the reference. The vertical arrows indicate the Fermi energy of the substrates interacting with RhB^+. The horizontal arrows show the HOMO–LUMO energy gap (values indicated below the arrows in eV) of the dye interacting with the substrates.

interaction. This means that the excited electron resides on the adsorbate while the excitation lasts. As a final test of the model, we performed a DFT vibrational analysis and calculated the Raman intensities of a free RhB^+ molecule. We also used the optimized geometry of RhB^+ and added one electron to form the neutral molecule RhB^0 that has an extra electron without relaxing the geometry. The simulated Raman spectra are shown in Figure S8 in the Supporting Information. The comparison of the simulated spectra with the Raman measurements shows that the experimental results could be interpreted as a mixture of RhB^+ and RhB^0, thus in good agreement with the proposed model of an excitation transfer to the adsorbed molecule.

In summary, we have proposed a controllable way to synthesize large-area Si-doped graphene sheets using MTMS/hexane solution as precursors. The size and shape of the resulting SiG sheets can be well tuned by a conformal growth on Cu foils. When compared to PG, the substitutional Si doping within graphene causes a significant increase of I_D/I_G and a decrease in the I_{2D}/I_G, which might be attributed to the slight local distortions of a graphene lattice induced by the Si atoms embedded in the lattice. Interestingly, no significant Raman peak position difference was observed between SiG and PG, which differs to the behaviors of other doped graphenes (e.g., B-doped and N-doped graphene). This indicates that the incorporation of silicon to the carbon network does not bring new charge carriers and is consistent with silicon substituting carbon in the trigonal arrangement, as in the *Si3* model calculation. Si-doped graphene can efficiently quench the fluorescence and thus enhance the Raman scattering of organic molecules. The theoretical modeling of SiG indicates that the substitution of

C by Si induces local curvature around the substitutional site, which also enhances the interaction of the tested dye molecules with graphene. The interacting orbitals of RhB^+ were shown to spread due to the increased interaction with Si-doped sites, thus providing a more effective mechanism of charge transfer between dye and substrate and an overall enhanced GERS signals. Our results will open up opportunities for developing high-performance sensors able to detect trace amount of organic and fluorescent molecules. In addition, many other fascinating properties predicted by theoretical calculations can now be tested based on the synthesis of high-quality SiG sheets.

Experimental Section

Synthesis of SiG Sheets: The synthesis of large-area SiG was achieved in a home-designed bubbler-assisted ambient-pressure chemical vapor deposition (AP-CVD) system operating at ambient pressure. Methoxytrimethylsilane (MTMS) ($C_4H_{12}OSi$, CAS No.: 1825–61–2, Aldrich) and hexane (C_6H_{14}) (CAS No.: 110–54–3, Purity > 99.0%, Sigma–Aldrich) were used as Si and C precursors, respectively. MTMS can also serve as C precursor in addition to hexane in the SiG growth. A typical run for SiG synthesis can be described as follows. Firstly, copper foils (99.8% purity, 25 μm thick, Alfa Aesar) were cleaned in a diluted HCl aqueous solution (HCl:H_2O = 1:3 v/v), dried with N_2 airbrush and then loaded into the AP-CVD quartz tubing reactor. Subsequently, the reactor was heated up to 1000 °C with the steps shown in Figure S1 in the Supporting Information and kept constant for 10 min. A mixture of Ar (1000 sccm) and H_2 (50 sccm) was used to remove the air inside the reactor before and during heating. After that, an MTMS/hexane solution was bubbled into the reactor by 1 sccm Ar gas at 1000 °C for 5 min. Finally, the reactor was cooled down to room temperature in an Ar flow (500 sccm). Two kind of control samples, PG and NG sheets were synthesized by using methane (CH_4) and ammonia (NH_3) as precursors. More experimental details including transfer, sample characterization, GERS measurements, computational details and additional figures can be found in the Supporting Information.

Supporting Information

Supporting Information is available from the Wiley Online Library or from the author.

Acknowledgements

R.L. acknowledges the support from the National Natural Science Foundation of China (Grant No. 51372131). M.T. thanks the U.S. Army Research Office MURI grant W911NF-11–1–0362 and JST-Japan for funding the Research Center for Exotic NanoCarbons, under the Japanese regional Innovation Strategy Program by the Excellence. M.T. also acknowledges support from the Penn State Center for Nanoscale Science for a seed grant on 2-D Layered Materials (DMR-0820404). The authors also acknowledge the Center for 2-Dimensional and Layered Materials. M.C.S. acknowledges FAPESP for financial support and the Research Computing and Cyber-infrastructure unit of Information Technology Services at Penn State University for providing access to the advanced computational facilities and services.

Received: August 4, 2014
Revised: September 22, 2014
Published online: October 29, 2014

[1] K. S. Novoselov, A. K. Geim, S. V. Morozov, D. Jiang, Y. Zhang, S. V. Dubonos, I. V. Grigorieva, A. A. Firsov, *Science* **2004**, *306*, 666.
[2] a) R. T. Lv, M. Terrones, *Mater. Lett.* **2012**, *78*, 209; b) H. Terrones, R. T. Lv, M. Terrones, M. S. Dresselhaus, *Rep. Prog. Phys.* **2012**, *75*, 062501.
[3] a) A. Das, S. Pisana, B. Chakraborty, S. Piscanec, S. K. Saha, U. V. Waghmare, K. S. Novoselov, H. R. Krishnamurthy, A. K. Geim, A. C. Ferrari, A. K. Sood, *Nat. Nanotechnol.* **2008**, *3*, 210; b) Y. B. Zhang, T. T. Tang, C. Girit, Z. Hao, M. C. Martin, A. Zettl, M. F. Crommie, Y. R. Shen, F. Wang, *Nature* **2009**, *459*, 820.
[4] J. E. Santos, N. M. R. Peres, J. dos Santos, A. H. C. Neto, *Phys. Rev. B* **2011**, *84*, 085430.
[5] R. H. Miwa, T. M. Schmidt, W. L. Scopel, A. Fazzio, *Appl. Phys. Lett.* **2011**, *99*, 163108.
[6] L. Y. Zhao, R. He, K. T. Rim, T. Schiros, K. S. Kim, H. Zhou, C. Gutierrez, S. P. Chockalingam, C. J. Arguello, L. Palova, D. Nordlund, M. S. Hybertsen, D. R. Reichman, T. F. Heinz, P. Kim, A. Pinczuk, G. W. Flynn, A. N. Pasupathy, *Science* **2011**, *333*, 999.
[7] W. J. Yu, L. Liao, S. H. Chae, Y. H. Lee, X. F. Duan, *Nano Lett.* **2011**, *11*, 4759.
[8] a) X. R. Wang, X. L. Li, L. Zhang, Y. Yoon, P. K. Weber, H. L. Wang, J. Guo, H. J. Dai, *Science* **2009**, *324*, 768; b) D. C. Wei, Y. Q. Liu, Y. Wang, H. L. Zhang, L. P. Huang, G. Yu, *Nano Lett.* **2009**, *9*, 1752; c) Z. Z. Sun, Z. Yan, J. Yao, E. Beitler, Y. Zhu, J. M. Tour, *Nature* **2010**, *468*, 549; d) R. Lv, Q. Li, A. R. Botello-Mendez, T. Hayashi, B. Wang, A. Berkdemir, Q. Z. Hao, A. L. Elias, R. Cruz-Silva, H. R. Gutierrez, Y. A. Kim, H. Muramatsu, J. Zhu, M. Endo, H. Terrones, J. C. Charlier, M. H. Pan, M. Terrones, *Sci. Rep.* **2012**, *2*, 586; e) J. Han, L. L. Zhang, S. Lee, J. Oh, K. S. Lee, J. R. Potts, J. Y. Ji, X. Zhao, R. S. Ruoff, S. Park, *ACS Nano* **2013**, *7*, 19; f) L. Zhao, M. Levendorf, S. Goncher, T. Schiros, L. Pálová, A. Zabet-Khosousi, K. T. Rim, C. Gutiérrez, D. Nordlund, C. Jaye, M. Hybertsen, D. Reichman, G. W. Flynn, J. Park, A. N. Pasupathy, *Nano Lett.* **2013**, *13*, 4659.
[9] P. A. Denis, *Chem. Phys. Lett.* **2010**, *492*, 251.
[10] H. Gao, Z. Liu, L. Song, W. H. Guo, W. Gao, L. J. Ci, A. Rao, W. J. Quan, R. Vajtai, P. M. Ajayan, *Nanotechnology* **2012**, *23*, 275605.
[11] S. Some, J. Kim, K. Lee, A. Kulkarni, Y. Yoon, S. Lee, T. Kim, H. Lee, *Adv. Mater.* **2012**, *24*, 5481.
[12] M. F. Chisholm, G. Duscher, W. Windl, *Nano Lett.* **2012**, *12*, 4651.
[13] a) W. Zhou, M. D. Kapetanakis, M. P. Prange, S. T. Pantelides, S. J. Pennycook, J. C. Idrobo, *Phys. Rev. Lett.* **2012**, *109*, 206803; b) Q. M. Ramasse, C. R. Seabourne, D. M. Kepaptsoglou, R. Zan, U. Bangert, A. J. Scott, *Nano Lett.* **2013**, *13*, 4989.
[14] P. A. Denis, *Chem. Phys. Lett.* **2011**, *508*, 95.
[15] Y. Chen, X. C. Yang, Y. J. Liu, J. X. Zhao, Q. H. Cai, X. Z. Wang, *J. Mol. Graphics* **2013**, *39*, 126.
[16] Y. Chen, Y. J. Liu, H. X. Wang, J. X. Zhao, Q. H. Cai, X. Z. Wang, Y. H. Ding, *ACS Appl. Mater. Interfaces* **2013**, *5*, 5994.
[17] J. H. Cho, S. J. Yang, K. Lee, C. R. Park, *Int. J. Hydrogen Energy* **2011**, *36*, 12286.
[18] a) Y. Zou, F. Li, Z. H. Zhu, M. W. Zhao, X. G. Xu, X. Y. Su, *Eur. Phys. J. B* **2011**, *81*, 475; b) Y. Chen, B. Gao, J. X. Zhao, Q. H. Cai, H. G. Fu, *J. Mol. Model.* **2012**, *18*, 2043.
[19] a) X. Ling, J. Zhang, *Small* **2010**, *6*, 2020; b) X. Ling, L. M. Xie, Y. Fang, H. Xu, H. L. Zhang, J. Kong, M. S. Dresselhaus, J. Zhang, Z. F. Liu, *Nano Lett.* **2010**, *10*, 553.
[20] L. M. Xie, X. Ling, Y. Fang, J. Zhang, Z. F. Liu, *J. Am. Chem. Soc.* **2009**, *131*, 9890.
[21] A. C. Ferrari, D. M. Basko, *Nat. Nanotechnol.* **2013**, *8*, 235.
[22] A. C. Ferrari, *Solid State Commun.* **2007**, *143*, 47.
[23] R. L. Schmitt, J. A. Gardella, J. H. Magill, R. L. Chin, *Polymer* **1987**, *28*, 1462.
[24] S. Grimme, *J. Comput. Chem.* **2006**, *27*, 1787.
[25] A. D. Becke, *J. Chem. Phys.* **1993**, *98*, 5648.